

AD-A086 005

SAGE ACTION INC ITHACA N Y

F/6 20/4

PREDICTION OF AERODYNAMIC LOADS ON CLOSE-COUPLED CANARD CONFIGU--ETC(U)

JUL 77 R W HALE, P TAN, D E ORDWAY

N00014-72-C-0200

UNCLASSIFIED

SAI-RR-7702

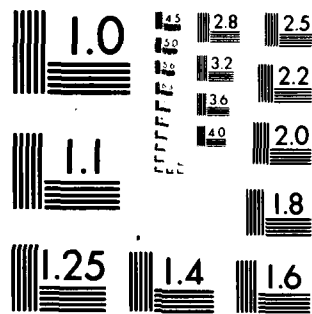
ONR-CR215-194-3F

NL

1 - 1  
A  
20/4/77



END  
DATE  
FILMED  
8 80  
DTIC



MICROCOPY RESOLUTION TEST CHART  
NATIONAL BUREAU OF STANDARDS 1963 A

ADA 086005

LEVEL 1A

(12)

DTIC  
F  
S JUN 25 1980  
C

12

ONR-CR215-194-3F  
SAI-RR 7702  
July 1977

PREDICTION OF AERODYNAMIC LOADS  
ON CLOSE-COUPLED CANARD CONFIGURATIONS -  
THEORY AND EXPERIMENT

by

R. W. Hale, P. Tan and D. E. Ordway  
SAGE ACTION, Inc.  
Ithaca, New York

DTIC  
ELECTE  
JUN 25 1980

Sponsored by:

Vehicles and Propulsion Program, Code 211  
Flight Vehicles Technology Division  
Office of Naval Research  
Arlington, Virginia 22217

Prepared under Contract N00014-72-C-0200,  
NR 215-194

Approved for public release; distribution unlimited.

#### Change of Address

Organizations receiving reports on the initial distribution list should confirm correct address. This list is located at the end of the report. Any change of address or distribution should be conveyed to the Office of Naval Research, Code 211, Arlington, VA 22217.

#### Disposition

When this report is no longer needed, it may be transmitted to other organizations. Do not return it to the originator or the monitoring office.

#### Disclaimer

The findings and conclusions contained in this report are not to be construed as an official Department of Defense or Military Department position unless so designated by other official documents.

#### Reproduction

Reproduction in whole or in part is permitted for any purpose of the United States Government.

# FOREWORD

This work was performed for the Office of Naval Research, Vehicles and Propulsion Program, Code 211, Flight Vehicles Technology Division, under ONR Contract N00014-72-C-0200. It was originally presented as Paper No. 9 at the AGARD Fluid Dynamics Panel Symposium, "Prediction of Aerodynamic Loading", NASA Ames, 27 - 29 September 1976. T. L. Wilson and R. E. Whitehead of the ONR served as technical monitors.

The authors would like to express their appreciation to A. D. Hammond and his Staff at the NASA Langley Research Center for the use of the V/STOL Research Wind Tunnel. In particular, we thank J. C. Wilson for sharing his wind tunnel time with us. Also, we are grateful to D. W. Lacey at the Naval Ship Research and Development Center (NSRDC) for discussing his research with us and suggesting a model configuration.

Accession For	
NTIS	<input checked="" type="checkbox"/>
DND TAB	<input type="checkbox"/>
Unannounced	<input type="checkbox"/>
Subscription	<input type="checkbox"/>
By	
Distribution	
Number of Copies	
Final	Special
A	

## TABLE OF CONTENTS

1. INTRODUCTION	1
2. APPROACH	3
3. FLOW VISUALIZATION	5
4. AERODYNAMIC DATA	11
5. CCC THEORY	18
6. CONCLUSIONS	27
REFERENCES	28

# 1 INTRODUCTION

It was recognized some time ago that vortex interaction effects are responsible for the nonlinear, high-lift capability of slender, low aspect ratio delta wings. As a consequence, most of our present knowledge of vortex interaction stems from extensive studies of the flowfields of such planforms. Recent results, though, have shown that wings of moderate aspect ratio and less sweepback can also exhibit high lift at extreme angles of attack if certain modifications are employed to create favorable vortex interaction. One such modification is the addition of a canard just ahead of the wing in the so-called close-coupled canard (CCC) configuration.

The CCC configuration was pioneered in Sweden over a decade ago and led to the successful development of the Saab Viggen. Interest on an international scale has grown since then. Recently, Israel demonstrated a new version of its Kfir fighter which incorporates close-coupled canards to improve its dogfight capability in air-to-air combat. Here in the United States, the Air Force is engaged in a Control Configured Vehicles Program, using canard surfaces on a F-4E. These surfaces are part of conventional and unconventional modes of control that are under evaluation to enhance the effectiveness of this aircraft. The Navy, too, has devoted considerable attention to canards for future V/STOL fighters, like the XFV-12A.

The principal advantages that the CCC configuration brings to an advanced air-superiority fighter are a high total lift capability at large angles of attack, along with reduced trim drag. These aerodynamic advantages lead to impressive gains in combat effectiveness through increased turning rates, rate-of-climb and acceleration. Specific excess power, from an energy management viewpoint, is significantly increased. Other attributes include improved handling qualities, low gust sensitivities, and better takeoff and landing performance.

The existing technology has been sufficient to define the aerodynamic potential of the CCC configuration for a range of specific configurations. A fairly comprehensive review of CCC work to date is given in Ref. 1. In brief, it was almost a decade after the studies by Saab in the early 1960's before further studies were pursued in the United States at NSRDC and NASA Langley. These studies involved mainly wind tunnel tests on several generalized research models and a modified F-4B model. Prior analytical investigations have been very limited, usually to low angles of attack or to delta planforms for both the canard and the wing. Lately, however, NASA Langley has been trying to extend the Polhamus analogy to more representative planforms at high angles of attack.

This relatively modest effort overall has not provided a fundamental under-



standing of the flow processes that contribute to the superior aerodynamic performance. That is, a basic description of the favorable vortex interaction between the canard and the wing is still lacking, especially in the high angle of attack regime. Consequently, it is not surprising that there is no analysis available yet to predict the aerodynamic performance of CCC configurations. The objective of the present investigation is to obtain a good physical understanding of the canard/wing flowfield at high angles of attack and build from this a simplified theory of the aerodynamic interaction.

## 2 APPROACH

At the outset, it was clear from existing experimental evidence that a CCC configuration achieves much of its lift at high incidence from vortex lift. This lift is generated as the direct result of flowfield vortices which intimately interact with the canard and wing surfaces. Knowledge of these vortices and corresponding aerodynamic data are essential in order to formulate a meaningful and realistic analysis. Therefore, a comprehensive investigation, including experimental and theoretical phases, was planned.

The four guidelines for the experimental phase of the investigation were:

- Use the technology developed for flow visualization with helium-filled bubbles to identify all of the key features of the interactive flowfield.
- Select a particular CCC configuration which has already demonstrated a significant favorable aerodynamic interaction.
- Make the model(s) fairly large and eliminate or minimize the effects of any fuselage contribution.
- Obtain a consistent set of force, moment and pressure data over a range in angle of attack with emphasis on high incidence.

Two separate test programs were necessary. Both were conducted in the NASA Langley V/STOL Research Wind Tunnel which has a test section 14.5' high, 21.75' wide and 50' long. It can be run either closed, slotted or open. The first test program concentrated solely on visualization of the flow over a semi-span model, mostly with the test section open. This gave an ideal, unobstructed view. For the force, moment and pressure data desired, the second test program utilized a sting-mounted, full-span model with different wall conditions. The flow visualization results and wing surface pressure data constitute important information not previously known for any CCC configuration.

For the theoretical phase of the investigation, three guidelines were established:

- Start with the simplest formulation of the flowfield that retains the key features observed and add refinements as required.
- Apply potential flow theory, incorporating suitable singularity distributions of vortex lines and sheets for the canard and the wing surfaces plus any free vortex systems.
- Adopt a proven numerical method as far as possible to solve the resulting integral equations.

This theoretical approach is more or less the same as that followed historical-

ly to attack the isolated delta wing problem. For now, the method must be semi-empirical. That is, the strength and geometry of the additional free vortex systems will be determined, a priori, from the experiments. Hopefully, the insight provided will eventually lead to a means to remove the need for empirical data, or to some procedure along the lines of the Polhamus analogy.

### 3 FLOW VISUALIZATION

The CCC configuration for this test program was taken from one of the NSRDC generalized research configurations<sup>2</sup>. It is representative of current and projected high-performance aircraft designs and exhibited the best high-incidence lift and drag characteristics.

Fig. 1 shows a three-view scale drawing of the half-span model. The wing has leading and trailing edge sweep angles of  $50^\circ$  and  $23.5^\circ$ , respectively, with a taper ratio of 0.151 and an aspect ratio of 3.90. The canard is half of a pure  $60^\circ$  delta planform, giving an aspect ratio of 2.31. During most of the test, the canard was located at a distance equal to 23% of the wing MAC above the wing plane. Longitudinally, the canard trailing edge overlapped the wing by 21% of the root chord. The canard surface area was approximately 29% of the wing area. This relatively high area ratio is due, primarily, to the absence of any fuselage.

The wing section also matched the NSRDC wing section, a NACA 64A008 airfoil laid out in a direction inclined  $25^\circ$  outward relative to the chordal direction or nearly normal to the trailing edge. For the canard, a flat plate section was selected. It was 0.48% thick at the root and had a semi-circular leading edge and blunt trailing edge.

The overall size of the model was dictated by flow visualization and Reynolds number considerations. For both, the largest practical size was desired. The semi-span finally chosen for the wing was 6.0' (1.83 m). This gave a wing MAC of 43.66" (1.11 m) and a wing reference area of  $18.48 \text{ ft}^2$  ( $1.72 \text{ m}^2$ ). Further description of the model is contained in Ref. 1.

The use of helium-filled bubbles which are neutrally-buoyant have proven to be an accurate, unique tool for flow visualization<sup>3</sup>. Basically, bubbles about  $1/8$ " (3 mm) in diameter are generated by a small probe, or head, at rates up to 500 bubbles per second. After emerging from the head, the bubbles quickly reach the freestream velocity and spread out substantially, even with low levels of tunnel turbulence. If the flowfield is not filled adequately, more bubbles may be introduced by extra heads. Three heads were adequate in this test program.

Still, streak photography was the principal means for recording the bubble trajectories. With a high-sensitivity vidicon, videotape recordings were also made to supplement the still photography and identify unsteady effects. Intense collimated lighting was provided by a searchlight array placed downstream within the tunnel, in line with the model.

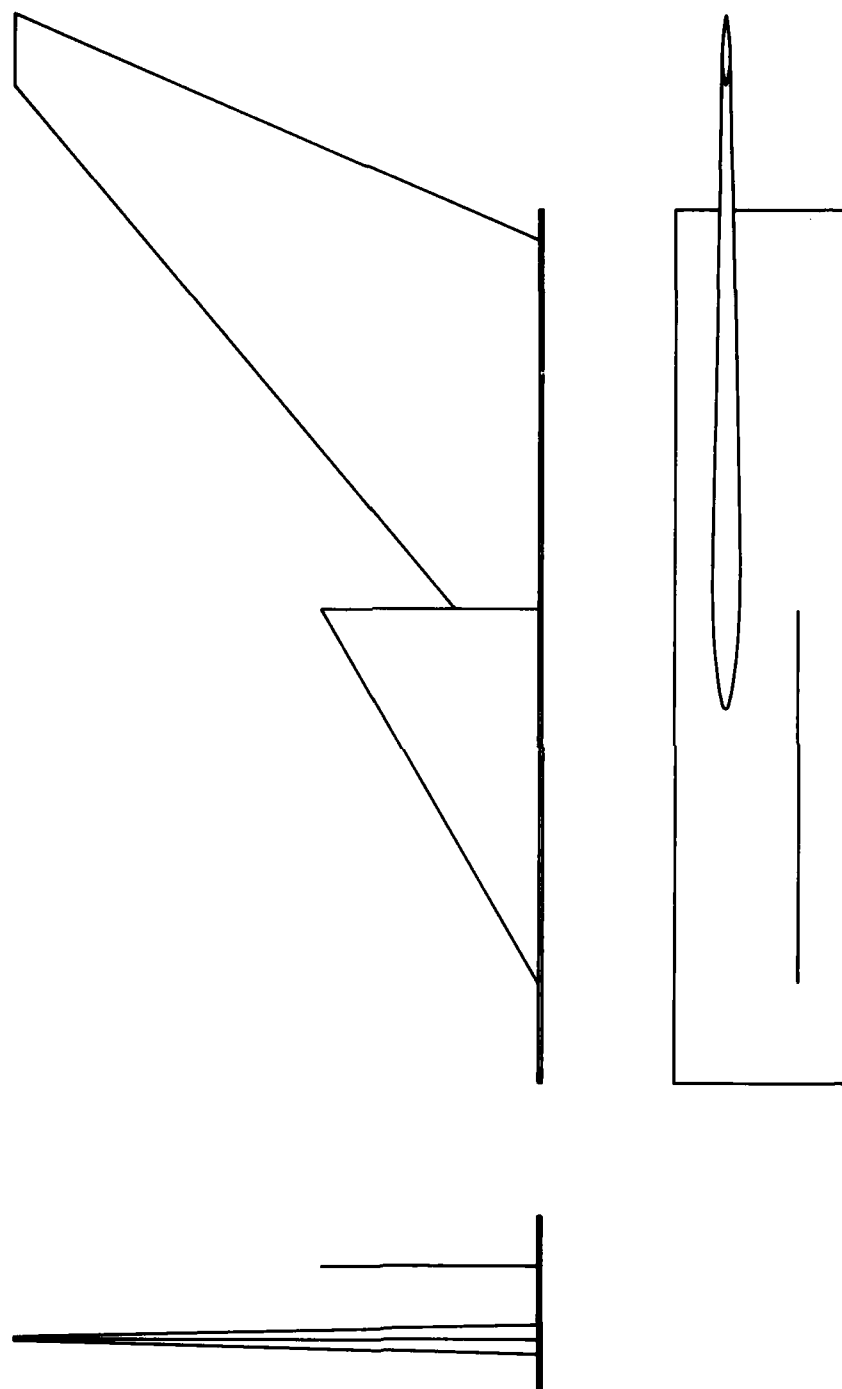


Figure 1. Three-View Drawing Of Semi-Span Close-Coupled Canard Model  
For Wind Tunnel Tests, Scale 1:24

Surface flow visualization was carried out in order to examine the boundary layer flows on the wing and canard as well. An oil flow technique with titanium dioxide was employed. The motions of the oil flow patterns were recorded by means of the video system.

The test plan was to concentrate on studying the model flowfield at a single angle of attack in the regime of favorable interaction. From the force data in Ref. 2, the angle decided upon was  $\alpha = 25^\circ$ . To compare the flow pattern at this angle with that at a much lower angle where the wing alone would not be stalled,  $\alpha = 10^\circ$  was tested, too. Most of the flow visualization was done at a Reynolds number of  $0.73 \times 10^6$ , based on the wing MAC. This is only slightly less than the value for the NSRDC data.

Two representative streak photographs for  $\alpha = 25^\circ$  are presented in Fig. 2, the upper one showing the wing without the canard and the lower one, with the canard. Without the canard, the wing is badly stalled and a turbulent separation region covers the whole upper surface. The rest of the flow goes smoothly around the separation region, which is fed by only a small streamtube close to the wing root. There is no evidence of an organized leading-edge vortex or a tip vortex.

Two important differences in the wing flowfield are apparent when the canard is installed. First, a tight leading-edge vortex is formed inboard that extends out to a distance about equal to the canard semi-span. This vortex is not evident in Fig. 2 since it is in a narrow shadow region. Shown dramatically, though, is the bursting of this vortex, the core becoming turbulent and enlarging as it passes over the wing and off the trailing edge. Outside this turbulent "funnel", the flow is laminar but it has appreciable rotation.

The second important feature is the unusual *spanwise flow* sandwiched between the burst vortex system and the upper surface of the wing. It starts inboard as flow which has gone over the leading-edge vortex and then reattached behind. After traveling underneath the burst vortex, it almost reaches the tip before turning back again into the freestream direction. No tip vortex is evident here either.

Although not shown in Fig. 2, the leading-edge vortex on the canard bursts near the apex, the same behavior that the canard alone would exhibit at this angle of attack. The core of this burst vortex is very turbulent and grows considerably as it moves rearward to the trailing edge and into the wake above the wing. It appears that the presence of the wing holds this burst trailing vortex system down near the canard and, thus, closer to the wing plane. Between the canard and wing, the flow is quite smooth, suggesting a "channeling" effect which preserves the leading-edge vortex on the inboard portion of the wing.

The surface flow visualization distinctly showed the separation line ahead of

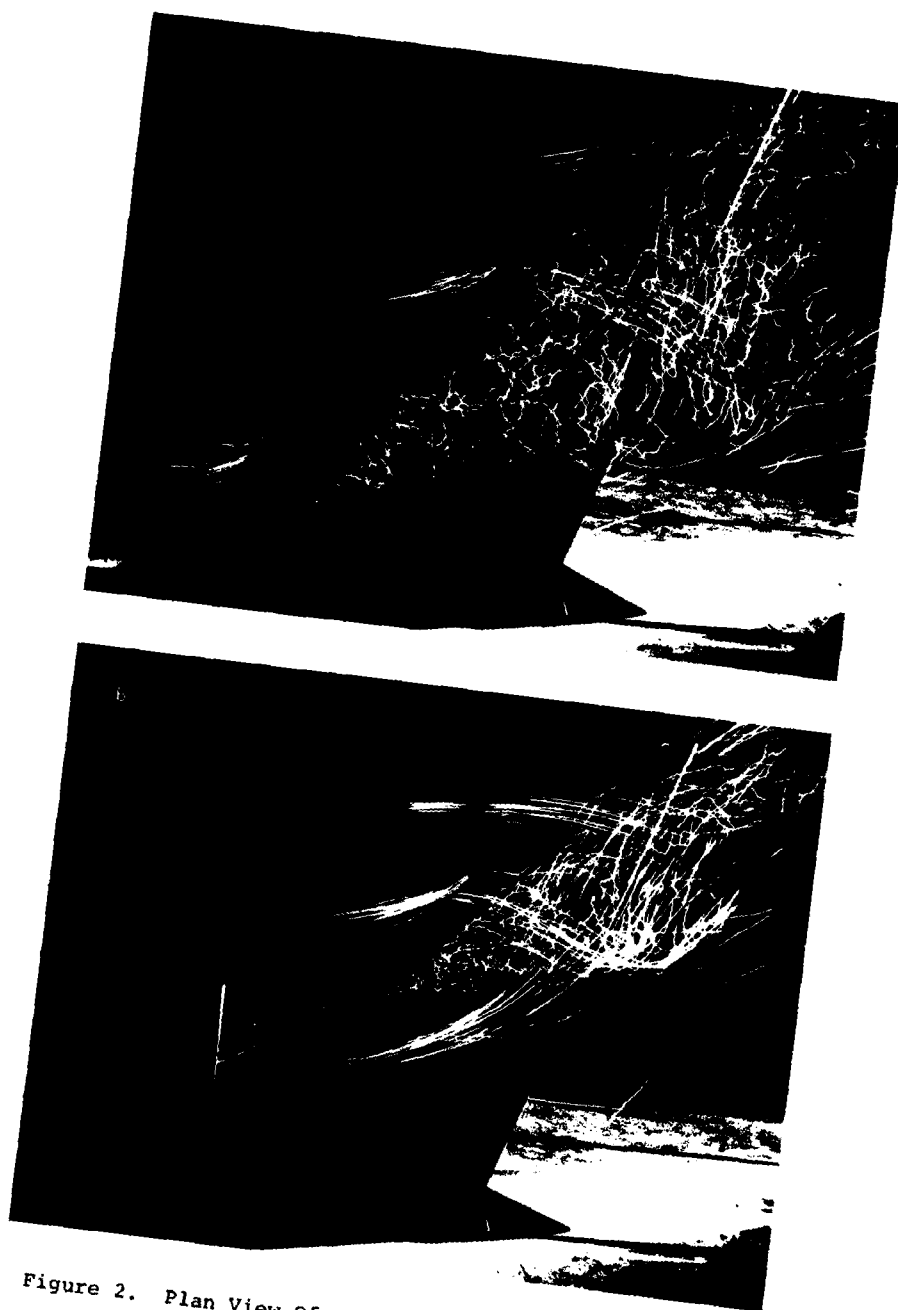


Figure 2. Plan View Of Flow Pattern Over Upper Surface  
Of Wing, With And Without Canard

the leading-edge vortex on the inboard portion of the wing. In many other places, however, a comparison of the surface patterns with the outer flow patterns revealed significant differences in flow direction. This indicates a drastic change in flow direction through the boundary layer.

At  $\alpha = 10^\circ$ , the vortex pattern over the wing without the canard is much like the pattern at  $\alpha = 25^\circ$  with the canard. The major difference lies in the absence of any noticeable spanwise flow. When the canard is added at this low angle of attack, there are no pronounced changes in the wing flowfield. Just the point of vortex bursting is displaced outboard slightly.

To extract an average or quasi-steady flowfield, a composite picture was constructed by superposition of streaks from a number of photographs. Considerable effort was needed to establish the three-dimensional relationship between the streaks. The end result for  $\alpha = 25^\circ$  is drawn in Fig. 3. The broad arrows describe the overall flow, which is steady and well ordered. The narrow arrows are actual bubble trajectories representative of the random motion in the burst vortex core.

It is fairly clear that the flow separates all along the wing leading edge, creating a leading-edge vortex sheet. This implies that there is no pressure difference or load across the wing at the leading edge, equivalent to the Kutta-Joukowski condition at the trailing edge. Inboard, the leading-edge vortex sheet rolls up tightly to form a concentrated vortex. Outboard, the sheet wraps around the turbulent core of the burst vortex as the core seems to detach from the wing surface. This causes the strong spanwise flow that was seen. It is important to distinguish this high-velocity spanwise flow *outside* the boundary layer from the low-velocity spanwise flow *inside* the boundary layer on yawed wings which has been recognized for some time. As a consequence, lower pressures are expected on the upper wing surface outboard and so more lift from the tip region at such high incidence.

By comparison, the inside of the burst vortex is nearly a dead-air region. The velocities are much lower and almost completely random, implying that the pressure is practically constant. The vortex sheet around this stagnant region is roughly conical in shape from the point of bursting to the wing trailing edge. These two properties of the burst vortex system greatly facilitate the theoretical formulation.



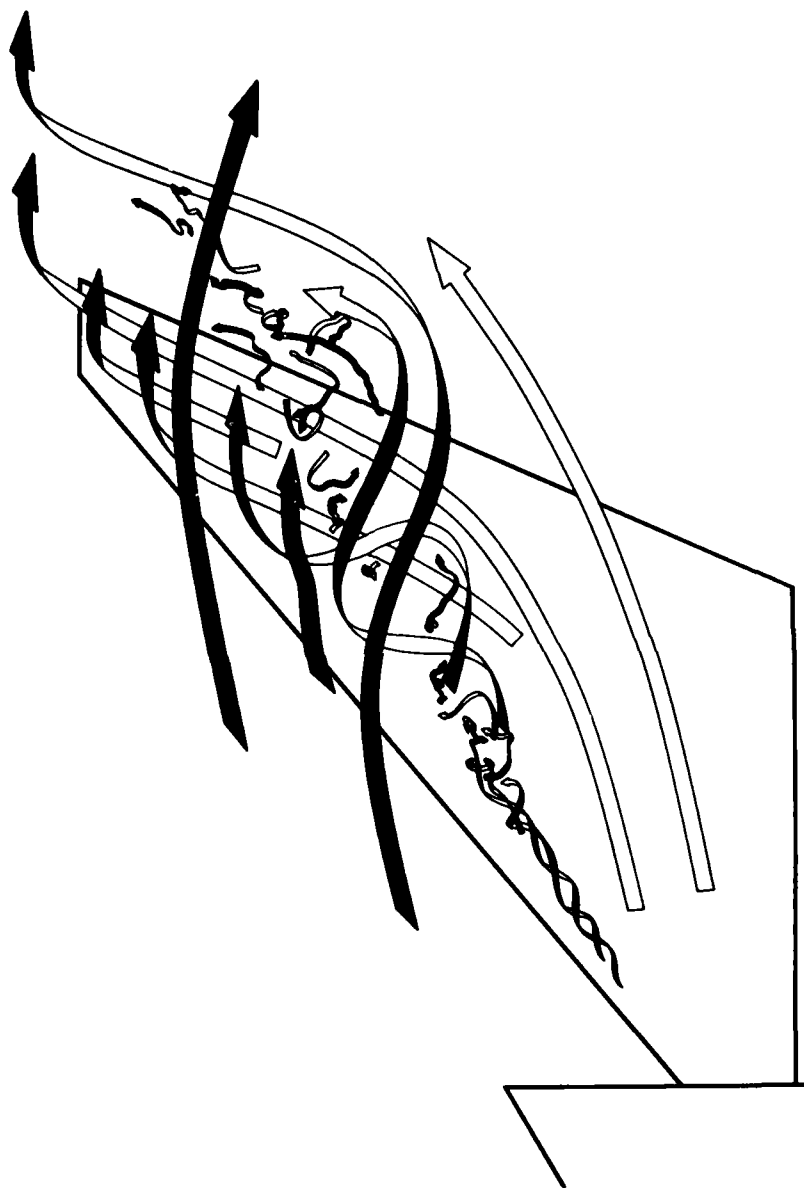


Figure 3. Composite Drawing Of Average Wing Flowfield  
For Close-Coupled Canard

## 4 AERODYNAMIC DATA

The full-span model for the second test program was built to the same scale as the semi-span model, or 12' (3.66 m) in span. Two small fuselages housed the internal balances, one to measure the total forces and moments, the other to measure just the canard loads. The upper surface of the right wing was instrumented with 61 pressure taps, most of them laid out at 7 spanwise and 9 chordwise locations. They were grouped more closely near the leading edge in the chordwise direction.

Full six-component force and moment data were taken by means of two sting knuckles over an extended range in  $\alpha$ , from  $0^\circ$  to  $36^\circ$ . Some flow visualization was also done to compare with the previous results. Altogether, four configurations were tested, the full CCC configuration, the wing-alone or wing plus body, the canard-alone or canard plus body, and the body by itself. In addition, the tunnel velocity was varied to assess the effects of Reynolds number. The Reynolds number based on the wing MAC ranged from approximately  $0.7 \times 10^6$  to  $3.7 \times 10^6$ .

The lift curve for the full CCC configuration is plotted in Fig. 4. It is seen that the lift coefficient increases monotonically, though not linearly, up to a value of over 1.8 referenced to the wing area. There is no indication of stall up to this point.

To evaluate the favorable aerodynamic interaction between the canard and wing, a second set of data points has been plotted for comparison. These points are for an "uncoupled" canard configuration in which the canard and wing act independently of each other. They were obtained by adding the lift coefficients for the wing-alone and canard-alone configurations, then subtracting the body-alone data. Only data for high angles of attack are shown because canard-alone and body-alone data were not taken at low angles. This uncoupled canard configuration stalls out between  $25^\circ$  and  $30^\circ$ .

As found by others, the curves cross over. Favorable interaction takes place above  $20^\circ$ , the lift increment between the close-coupled and the uncoupled canard configuration increasing with angle of attack. Below  $20^\circ$ , the uncoupled lift is a little higher.

This behavior can be explained by examination of the individual contributions of the wing and canard. The wing-alone data are shown in Fig. 5. The initial lift curve slope for the wing in the CCC configuration is appreciably less than for the wing alone. This should be anticipated from classical wing theory because of the downwash at the wing from the canard. By  $16^\circ$ , the lift curve slopes are about equal. The wing-alone lift peaks out at  $25^\circ$ , while the lift

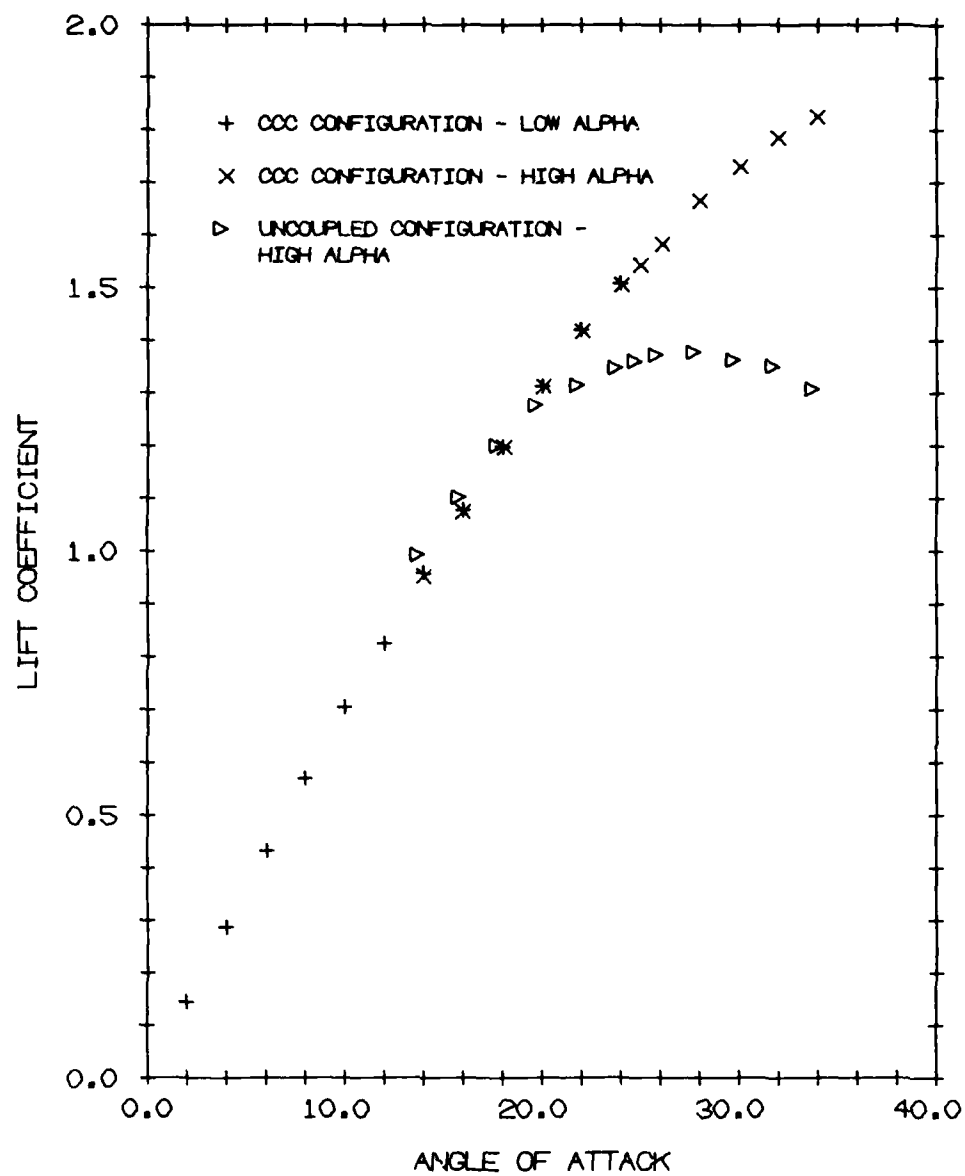


Figure 4. Comparison Of Close-Coupled Canard And Uncoupled Canard Lift Data

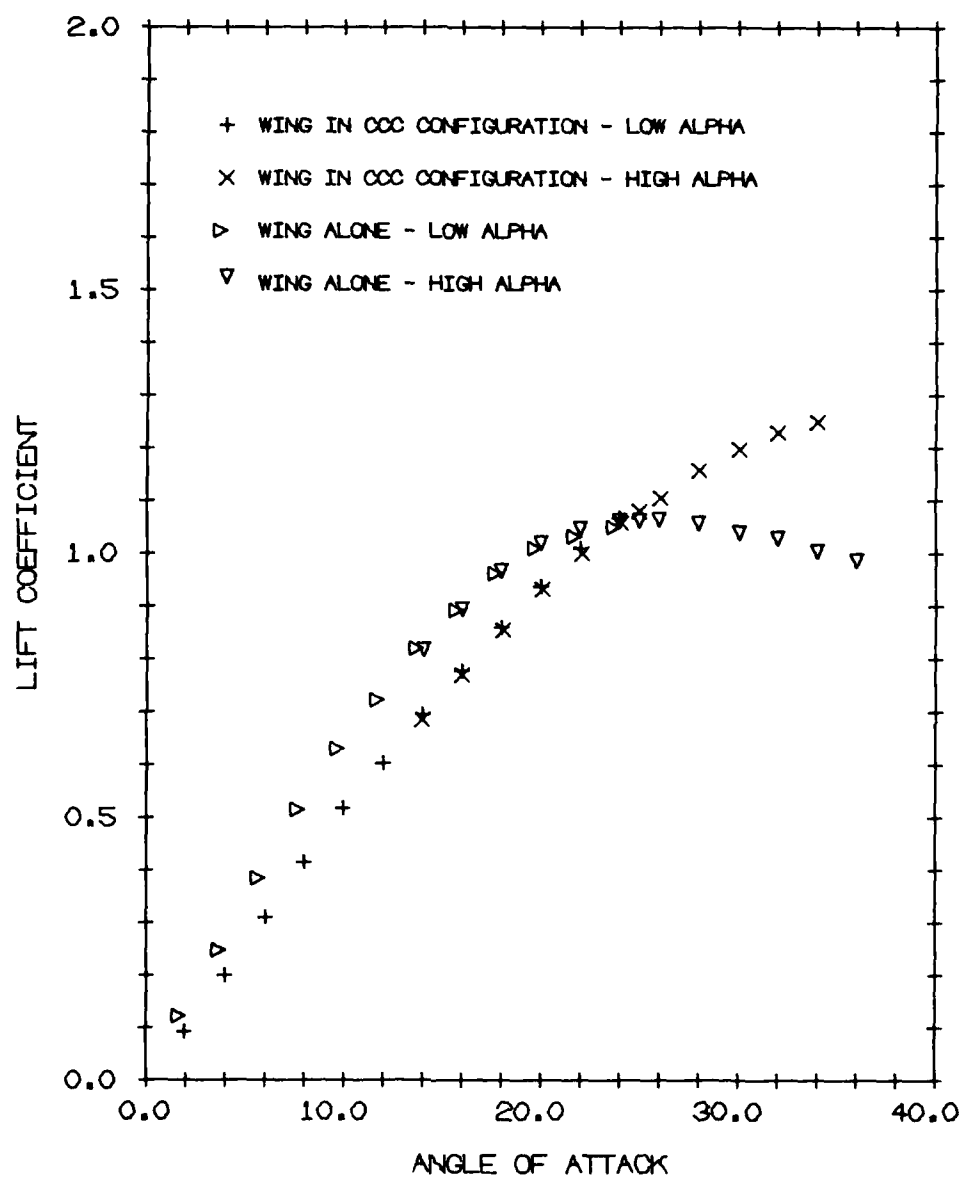


Figure 5. Comparison Of Lift Data For Wing Alone And In CCC Configuration

generated by the wing in the presence of the canard continues to climb, although at a declining rate. In boundary layer terminology, the canard appears to inhibit or delay stalling of the wing at high angles as substantiated by Fig. 2.

The canard-alone data are shown in Fig. 6, the lift coefficients again referenced to the wing area. They can be multiplied by the wing/canard area ratio of 3.399 to refer them to the canard area if desired. Extrapolating these data to the origin, the lift curve slope there is less than for the canard in the CCC configuration. As before, this should be anticipated from classical wing theory because of the upwash at the canard from the wing. Over the entire angle of attack range, the lift and lift curve slope for the canard in the presence of the wing is greater than for the canard alone. At 30°, the canard-alone lift reaches a maximum, indicating stall, but the canard lift in the CCC configuration still increases. Clearly, the improvement in canard lift at low angles from favorable interaction with the wing does not fully offset the reduction in wing lift. At high angles, though, the interaction is favorable to both surfaces.

It is significant to note that the canard develops more lift above 20° coupled to the wing than the maximum lift which the canard alone develops. There is no way to account for this by a change in the effective angle of attack of the canard due to the upwash from the wing. Instead, a change in the effective camber would have to be introduced or, perhaps, something more profound.

It is also significant to note that the high-angle data of Fig. 6 for the canard in the CCC configuration can be fitted extremely well by the Polhamus lift equation for delta wings<sup>4</sup>. If the coefficients are adjusted to match the measured values of  $C_L$  at 16° and 32°, the equation

$$C_L = 0.974 \sin \alpha \cos^2 \alpha + 0.777 \sin^2 \alpha \cos \alpha \quad (1)$$

predicts the measured values at all other angles of attack from 14° to 34° within 0.5%. Multiplying the constants in Eq. (1) by 3.399, they can be compared with the values of  $K_p$  and  $K_v$  in Ref. 5 for a 60° delta wing. The potential lift, or first term above, is 37% higher than given by the Polhamus analogy for an isolated delta wing. On the other hand, the vortex lift, or second term above, is 18% lower. Nonetheless, the fact that this lift equation derived from the Polhamus analogy is so good is very encouraging from a theoretical viewpoint.

With respect to Reynolds number effects, the lift data were repeatable over the whole range in Reynolds numbers covered in the test program. This is also encouraging because it indicates that any flowfield model which is adopted can be used with some generality.

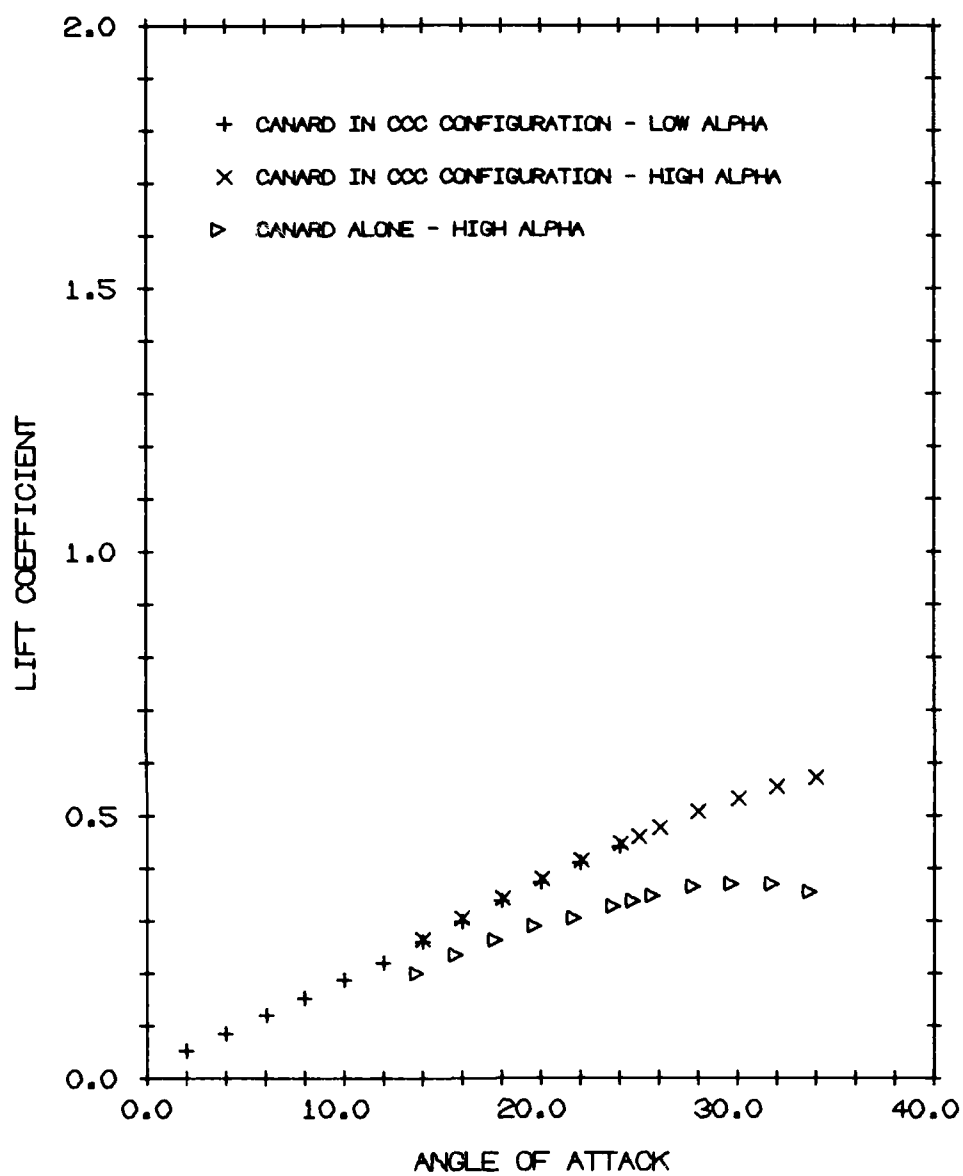


Figure 6. Comparison Of Lift Data For Canard Alone And In CCC Configuration

The flow visualization results agreed on the whole with the results from the first test program. Only the geometry of the burst vortex on the wing was slightly different. The included angle was somewhat larger. Also, the upstream edge of the burst vortex moved forward and became almost parallel to the leading edge. At the two angles of observation,  $25^\circ$  and  $32^\circ$ , the leading edge vortices on the canard were fully burst as seen in the semi-span tests. This may be the reason for the lower vortex lift from Eq. (1).

A sample of the pressure data is illustrated in Fig. 7 as contour lines of constant pressure coefficient over the upper surface of the wing. Contours for coefficient values of -0.5, -1, -2, -3 and -4 were chosen. Inboard, the contours are close together near the leading edge under the leading edge vortex. Outboard, the contour lines for -1 and -2 are "pulled" outward and rearward by the burst vortex system. The extreme points of these curves lie almost directly under the centerline of the burst system. These low pressures must be created by the high-velocity spanwise flow. Inboard or outboard, the shape of the contour lines do not change a great deal over the range of high angles of attack. This shows once more the persistence of the flowfield pattern.

Some comments should be made, finally, regarding tunnel wall effects. At the suggestion of NASA, the full CCC configuration was tested with the wind tunnel test section closed, slotted and open. The closed test section, which was used in all other runs, gave the highest lift values. With the slotted test section, both the total lift and the canard lift were 4% to 6% lower over the high-angle range. With the open test section, i.e. raising the two walls and ceiling, these lift values were 9% to 12% lower. Wall corrections are evidently needed, but the normal corrections did not give reasonable answers. The theoretical analysis should enable the derivation of appropriate corrections for this configuration.

The canard lift values with the tunnel slotted and open were also fitted very well by the Polhamus lift equation. Surprisingly, the potential lift of Eq. (1) for the test section closed was essentially unchanged. The lift reduction in both cases, therefore, came entirely in the vortex lift. Compared to the theoretical value for an isolated delta wing, as before, the vortex lift dropped from a value 18% lower with the closed test section to 35% lower with the slotted test section and down to 47% lower with the open test section.

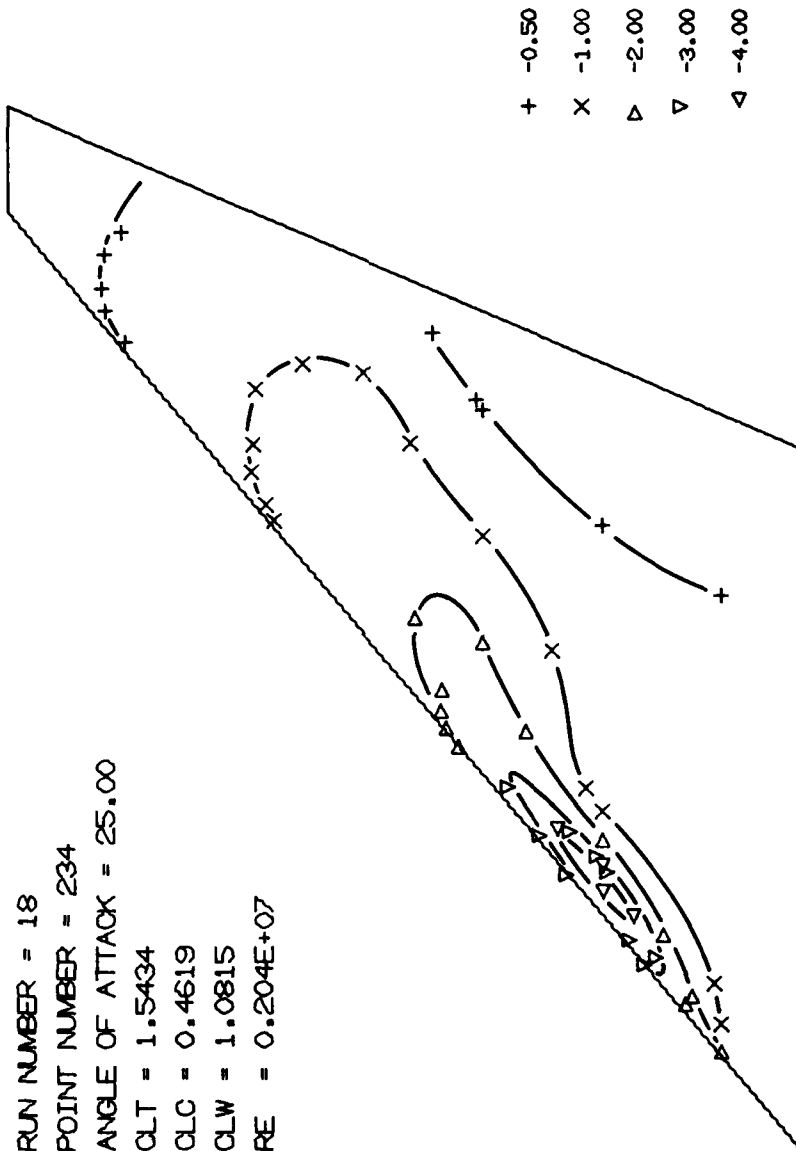


Figure 7. Pressure Distribution Over Upper Surface Of Wing  
In CCC Configuration



## 5 CCC THEORY

To construct a simplified theory for such a complex and unusual flowfield is a formidable challenge. Before proceeding, though, it is necessary to examine two aspects of the flowfield first in some detail. One is the spanwise flow and the other, the burst vortex system above the wing.

The upper sketch of Fig. 8 illustrates the velocity vectors for a representative point on the wing and the associated vorticity required to replace the wing by a vortex sheet. This point is located at the mid-chord, directly under the centerline of the burst vortex. The vector  $q_1$  lies in the direction of the spanwise flow above the wing, while  $q_2$  lies in the direction of the chordwise flow observed directly under the wing. The relative magnitude of these vectors were determined from the upper surface pressure coefficient of Fig. 7 and an estimate of the lower surface pressure coefficient. The "sheet" velocity  $q_s$  is the mean of  $q_1$  and  $q_2$ .

The local vorticity  $\gamma$  required to induce this change in velocity across the sheet is given by the vector equation

$$\gamma = - (q_1 - q_2) \times \underline{n} \quad (2)$$

where  $\underline{n}$  is the upward facing unit vector normal to the wing plane. Surprisingly,  $\gamma$  is pointed almost in the chordwise or streamwise direction. The bound vorticity in classical wing theory is usually pointed in the spanwise direction.

In a similar fashion, the jump conditions can be found for a vortex sheet around the burst vortex that will insure essentially stagnant flow inside. The vectors involved in this case are shown in the lower sketch of Fig. 8 for a point on the upper side of the burst system taken above the previous point. The velocity vector  $q_1$  outside the sheet was determined by flow visualization. If  $q_2 = 0$  immediately inside the sheet,  $q_s = q_1/2$  and  $\gamma$  follows from Eq. (2). The required vorticity here on the sheet has components both in the circumferential and ray directions on the burst vortex.

With this understanding in hand, a theoretical model can be formulated. This model is drawn in schematic form in Fig. 9. For the canard and wing, conventional horseshoe vortices are used. The burst vortex system above the wing is idealized as a cone, composed of ring vortices plus "cranked" horseshoe vortices. The ring vortices account for the circumferential component of the vorticity vector on the burst vortex sheet. The cranked horseshoes, depicted in Fig. 9 by a single horseshoe, are composed of three parts. On the burst vortex sheet, the conical elements account for the ray component of the vor-

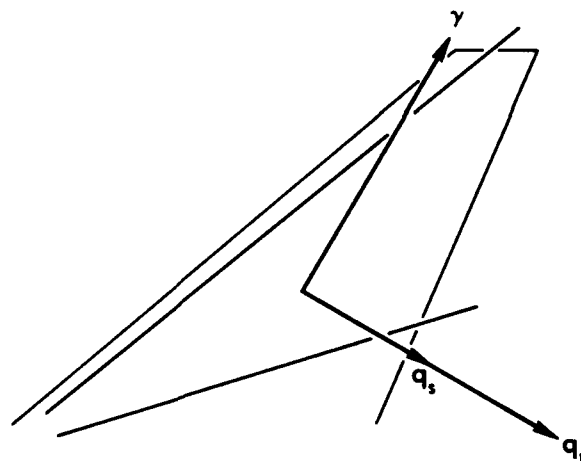
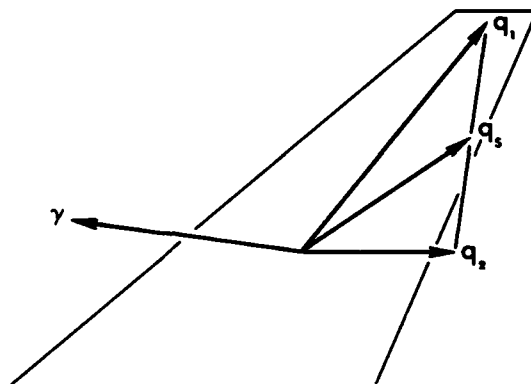


Figure 8. Velocity/Vorticity Vector Diagrams For Wing And Burst Vortex Sheets



ticity vector. These elements are smeared around the cone but are fed at only one azimuth by the umbilical elements from the wing leading edge. The umbilical elements, in turn, join the wing plane elements which may be skewed somewhat inboard or outboard. The wing plane elements are very important to vortex lift, as discussed later on.

The potential flow for present purposes will be defined as the regular attached flow in the absence of the burst vortex system. To determine this flow, the normal component of velocity must vanish everywhere on the wing and the canard. If the surfaces are parallel and uncambered, it follows then that

$$U \sin \alpha + w_{ww} + w_{wc} = 0 \quad (3)$$

$$U \sin \alpha + w_{cc} + w_{cw} = 0 \quad (4)$$

The velocity  $w_{ww}$  is the upwash on the wing induced by the vortex system of the wing,  $w_{wc}$  is the upwash on the wing induced by the vortex system of the canard,  $w_{cc}$  is the upwash on the canard induced by the vortex system of the canard and  $w_{cw}$  is the upwash on the canard induced by the vortex system of the wing. Eqs. (3) and (4) are exact for arbitrary  $\alpha$  within this formulation.

These equations constitute a set of integral equations coupled through  $w_{wc}$  and  $w_{cw}$ . They can be effectively decoupled and solved in closed form by successive iteration using operators. The final solutions may be expressed as

$$\gamma_w = \sum_{v=0}^{\infty} O_w^v \{ \gamma_w^{(0)} + \gamma_w^{(1)} \} \quad (5)$$

$$\gamma_c = \sum_{v=0}^{\infty} O_c^v \{ \gamma_c^{(0)} + \gamma_c^{(1)} \} \quad (6)$$

where  $\gamma_w$  is the strength of the unknown horseshoe vortex distribution on the wing and  $\gamma_c$ , the strength on the canard. The operators  $O_w$  and  $O_c$  are fairly complex operators given by the product of four other operators, two corresponding to the inversion of Eqs. (3) and (4) with no interaction and two, to the upwash of these surfaces on each other. With respect to the remaining terms,  $\gamma_w^{(0)}$  is the vortex strength on the isolated wing and  $\gamma_c^{(0)}$ , on the isolated canard. The other vortex strengths,  $\gamma_w^{(1)}$  and  $\gamma_c^{(1)}$ , arise from just the upwash induced by the vortex distributions for the isolated surfaces.

Any one of several computational methods for lifting surfaces in potential flow could be utilized to carry out the solutions of Eqs. (5) and (6) numerically. The Douglas EVD Method<sup>6,7</sup> was selected here. Since it was limited to vortex panels in a single plane, this method had to be generalized to include the

influence of out-of-plane panels.

The calculations for the influence of the burst vortex sheet are considerably simplified if the induced flowfield is conical. This can be achieved by assuming a constant distribution of vorticity and extending the conical sheet from the apex to infinity. Then the induced velocities are constant along rays or concentric cones.

A cylindrical coordinate system  $(x, r, \theta)$  is employed with the origin at the apex and the x-axis along the cone axis. The circumferential vorticity  $\gamma_\theta$ , or distribution of ring vortices, induces an axial velocity component  $u$  and a radial velocity component  $v$ . The  $\theta$ -integration of the Biot-Savart law can be performed analytically in terms of Legendre functions of the second kind and half-integer order  $Q_{n-1/2}$ . If the conical variables  $\eta \equiv x/r$  and  $\eta_v \equiv x_v/r_v$  are used to indicate the rays on which the field point  $(x, r)$  and vortex points  $(x_v, r_v)$  are located, the results can be reduced to the form shown in Table 1. On the other hand, the ray vorticity  $\gamma_\eta$  induces only a circumferential velocity component  $w$ . It can be reduced like  $u$  and  $v$  and is included along with them in Table 1.

This leaves the umbilical elements and the wing plane elements of the cranked horseshoe vortices. Since the influence of the umbilical elements should be small, these elements will be neglected. The wing plane elements, though, will play a pivotal role. This role will be discussed further in a moment.

With regard now to numerical results for the potential lift, calculations were performed for the canard alone, wing alone and the full CCC configuration. These were run on a Modcomp II/220 Computer, taking a Glauert or cosine spacing of the EVD panels in both the spanwise and chordwise directions. In general, the agreement with other theoretical and experimental data, as well as with the present experimental data, is very good.

For the canard alone, the computed values of  $C_L / \sin \alpha$  range from 2.51 to 2.62. These values correspond to  $12 \times 6$  and  $6 \times 6$  arrays of EVD panels, respectively, where the first integer is the number of panels counted in the spanwise direction and the second integer, in the chordwise direction. Values from Refs. 4 and 5 for other lifting surface methods are 2.45 and 2.41, by comparison, or about 5% less. The experimental values reported in Ref. 8 for low angles are 2.58 and 2.61, or exceptionally close to the theoretical values, while the value of 2.75 from Ref. 9 is a little high.

For the wing alone, the computed values of  $C_L / \sin \alpha$  range from 3.29 to 3.50. The lowest value corresponds to an  $18 \times 6$  array and the highest value, to a  $6 \times 6$  array. The present experimental data at low angles, see Fig. 5, fall between 3.44 and 3.55 with the test section closed. This is somewhat higher than the theoretical predictions, as might be expected from the tunnel interference

$$u / \gamma_{\theta} = F_1 \int_0^{\infty} \{ \eta_v \xi Q_{-1/2}^i(\omega) - \eta Q_{1/2}^i(\omega) \} / \xi^{1/2} d\xi \quad (7)$$

$$v / \gamma_{\theta} = F_1 \int_0^{\infty} (1 - \xi) Q_{1/2}^i(\omega) / \xi^{1/2} d\xi \quad (8)$$

$$w / \gamma_{\eta} = F_2 \int_0^{\infty} \{ \eta_v Q_{1/2}^i(\omega) - \eta Q_{-1/2}^i(\omega) \} / \xi^{1/2} d\xi \quad (9)$$

$$F_1 \equiv (1 + \eta_v^2)^{1/2} / 2\pi\eta (\eta\eta_v)^{1/2} \quad (10)$$

$$F_2 \equiv 1 / 2\pi\eta (\eta\eta_v)^{1/2} \quad (11)$$

$$\omega \equiv 1 + \{ (1 - \xi)^2 + (\eta - \eta_v \xi)^2 \} / 2\eta\eta_v \xi \quad (12)$$

Table 1. Equations For Velocity Components Induced  
By Conical Vortex Sheet

discussed earlier. An estimate of the comparable values for a slotted test section are 3.28 to 3.39, agreeing quite well with the calculated results. A value of 3.39 was obtained from the NSRDC data in Ref. 2.

Computer runs for the full CCC configuration were made with two sets of EVD panel layouts. One, with a 12 x 6 array on the wing and a 6 x 6 array on the canard, gave a value for  $C_L / \sin \alpha$  based on the wing area of 3.71. The other, with 15 x 6 and 9 x 6 arrays, instead, gave a slightly higher value of 3.73. By comparison, the present test data at low angles varied from 3.80 to 3.95 with the test section closed and from 3.64 to 3.73 with the test section slotted.

Numerical results for the velocities induced by the burst vortex sheet  $u/\gamma_\theta$ ,  $v/\gamma_\theta$  and  $w/\gamma_\eta$  are plotted in Fig. 10. These values were found by numerical integration of Eqs. (7), (8) and (9) for a semi-vertex angle of  $11^\circ$  as measured from flow visualization photographs. Careful examination of Eq. (7) reveals that this integral is actually slowly divergent. Therefore, the numerical integration was cut off at  $\xi = 50$ .

The position of the vortex sheet  $\eta_v$  is denoted by the dashed line in Fig. 10. Directly outside the sheet, the dimensionless axial, radial and circumferential velocities are -0.128, 0.191 and 1.000, respectively. Inside the sheet,  $u/\gamma_\theta$  is approximately equal to -1.110 everywhere and the other two components identically vanish. These values satisfy the correct jump conditions across the sheet of  $\cos 11^\circ$ ,  $\sin 11^\circ$  and 1.000, respectively.

To qualify the theoretical model of the burst vortex system up to this point, particle trajectories were computed for the flow about the conical vortex sheet placed in a uniform stream. The magnitude of the stream velocity was chosen to cancel  $u$  inside the sheet and the ratio of  $\gamma_\theta$  to  $\gamma_\eta$  was taken from the flow inclination measured just outside the upper surface of the burst vortex, see Fig. 8. Under these conditions, the conical vortex sheet simulates a solid cone so there is no flow through the sheet.

Several different "starting points" were tried for the "particles" and the trajectories superimposed upon photographs of the actual bubble traces. In certain areas, some local discrepancies exist, such as close to the upper wing surface. Overall, though, the shape and behavior in the two cases are remarkably alike.

Once the flowfield model for the burst vortex system has been established, the final steps of development of the theory can be undertaken. The first thing that has to be done is the computation of the additional downwash contributions. With empirical values for  $\gamma_\theta$  and  $\gamma_\eta$ , the contributions of the ring vortices and the ray elements of the cranked horseshoe vortices can be readily calculated from  $u$ ,  $v$  and  $w$ . Since the contribution of the umbilical elements of the cranked horseshoe vortices will be neglected, only the contribution of

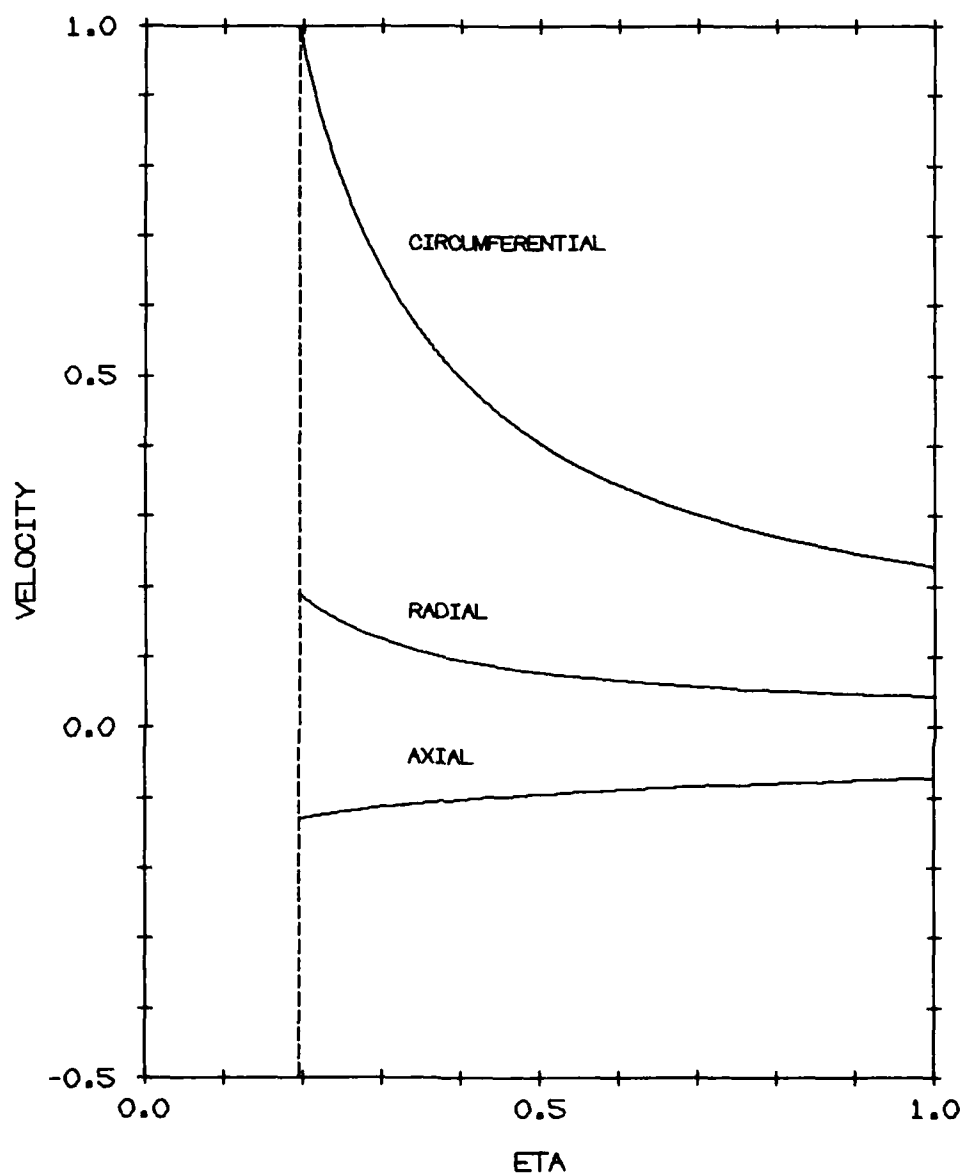


Figure 10. Velocity Components Induced By Burst Vortex Sheet



the wing plane elements is needed. This can be carried out in the manner of lifting-line theory after the skew angle has been fixed.

With the additional downwash contributions computed,  $w_{ww}$  and  $w_{cw}$  in Eqs. (3) and (4) can be adjusted and new distributions of  $\gamma_w$  and  $\gamma_c$  determined from Eqs. (5) and (6). The operators  $\partial_w$  and  $\partial_c$  will have to be changed for this purpose by suppressing the leading edge singularity. Also, the numerical implementation will have to be changed, but the explicit identification of this singularity in the Douglas EVD Method should facilitate this change.

The last step of development of the theory will be the computation of the surface pressures and the resultant lift. To do this, the total surface velocities will be found, then substituted into the full Bernoulli equation and integrated. It can be seen immediately that the "lift mechanism" will be quite different. That is, besides the lift produced by the product of the X-component of the surface sheet velocity and the Y-component of the vorticity, there will be lift due to the product of the Y-component of the surface sheet velocity and the X-component of vorticity.

This latter lift depends strongly upon the wing plane elements of the cranked horseshoes vortices. In fact, it constitutes most of the vortex lift, or lift increment in the presence of the burst vortex system. Judged from Fig. 8, the vortex lift will dominate the potential lift over much of the wing at high angles of attack.

## 6 CONCLUSIONS

Based upon the progress to date of a comprehensive investigation to develop a simplified theory for the close-coupled canard configuration, the following conclusions are drawn:

- A detailed understanding of the flowfield for a representative configuration has been obtained on a 6' (1.83 m) semi-span model by flow visualization.
- Three prominent features of the flow have been identified. One is the presence of a large, well-ordered burst vortex above the wing at high angles of attack. Another is the strong spanwise flow which is sandwiched between this vortex and the wing at these angles. The third is the apparent constraint of the canard vortex system that greatly improves the canard lift characteristics.
- Corresponding aerodynamic measurements have been taken on a 12' (3.66 m) full-span model, including pressure contours on the upper surface of the wing. These contours clearly correlate with the burst vortex observed.
- Highly-favorable interaction was achieved with lift values over 1.8 reached at  $\alpha = 34^\circ$  without stall. The canard lift has been fitted within 0.5% variation, over the whole high-angle range tested, with the Polhamus lift equation by adjusting the coefficients.
- The proper velocity/vorticity relationships for both the wing and the burst vortex have been derived and a mathematical model has been formulated. This involves besides the usual singularities the addition of ring vortices and cranked horseshoe vortices to represent the burst vortex system.
- Two other key steps have been completed. The potential lift has been found in closed form for arbitrary angles of attack. Also, the influence of the most difficult parts of the burst vortex system has been reduced to a conical form which is very convenient for computations.
- Both steps have been qualified numerically. Lift results calculated for low angles by extending the Douglas EVD Method show excellent agreement overall with other theoretical and experimental data, as well as with the present experimental data. Particle trajectories of the flow about the idealized burst vortex in a uniform stream have been computed, too, and compare well with the actual trajectories seen.
- At high angles of attack, the vortex lift clearly dominates the potential lift. Some work remains to be done, but the mechanism for this lift has been determined.

## REFERENCES

1. Hale, R. W. and Ordway, D. E., High-Lift Capabilities from Favorable Flow Interaction with Close-Coupled Canards, Sage Action, Inc., SAI-RR 7501, December 1975.
2. Krouse, J. R., Effects of Canard Planform on the Subsonic Aerodynamic Characteristics of a 25° and a 50° Swept-Wing Research Aircraft Model, NSRDC Evaluation Report AL-91, May 1972.
3. Hale, R. W., Tan, P., Stowell, R. C. and Ordway, D. E., Development of an Integrated System for Flow Visualization in Air Using Neutrally-Buoyant Bubbles, Sage Action, Inc., SAI-RR 7107, December 1971; AD-756 691.
4. Polhamus, E. C., A Concept of the Vortex Lift of Sharp-Edge Delta Wings Based on a Leading-Edge-Suction Analogy, NASA TN D-3767, December 1966.
5. Polhamus, E. C., Charts for Predicting the Subsonic Vortex-Lift Characteristics of Arrow, Delta, and Diamond Wings, NASA TN D-6243, April 1971.
6. Lopez, M. L., Shen, C. C. and Wasson, N. F., A Theoretical Method for Calculating the Aerodynamic Characteristics of Arbitrary Jet-Flapped Wings; Volume I, The Elementary Vortex Distribution Jet-Wing Lifting Surface Theory, Douglas Aircraft Company, Report No. MDC J5519-01, May 1973.
7. Lopez, M. L., Shen, C. C. and Wasson, N. F., A Theoretical Method for Calculating the Aerodynamic Characteristics of Arbitrary Jet-Flapped Wings; Volume II, EVD Jet-Wing Computer Program User's Manual (CDC 6000 Series Computers), Douglas Aircraft Company, Report No. MDC J5519-02, May 1973.
8. Jones, R. and Miles, C. J. W., Tests on Three Equilateral Triangular Plates in the Compressed Air Tunnel, A.R.C. R. & M. No. 2518, 1952.
9. Wentz, W. H., Jr. and Kohlman, D. L., Wind Tunnel Investigations of Vortex Breakdown on Slender Sharp-Edged Wings, University of Kansas Center for Research, Inc., Engineering Sciences Division, Report FRL 68-013 (Also NASA CR-98737), November 1968.

# DISTRIBUTION LIST

7	Chief of Naval Research Department of the Navy Arlington, Virginia 22217 Attn: Code 211	(7)
2	Chief of Naval Development Department of the Navy Washington, D. C. 20360 Attn: NAVMAT 0331 NAVMAT 0334	(1) (1)
1	Naval Air Systems Command Department of the Navy Washington, D. C. 20361 Attn: NAVAIR 320D	(1)
2	Naval Ship Research & Development Center Aviation and Surface Effects Department Bethesda, Maryland 20084 Attn: Director, Code 16 Library, Code 5643	(1) (1)
9	Naval Research Laboratory Washington, D. C. 20375 Attn: Technical Information Office, Code 2627 Library, Code 2629	(6) (3)
1	Superintendent U. S. Naval Academy Annapolis, Maryland 21402	(1)
1	Superintendent U. S. Naval Postgraduate School Monterey, California 93940	(1)
1	U. S. Naval Air Development Center Johnsville, Warminster, Pennsylvania 18974 Attn: Aeromechanics Department	(1)
1	Commandant of the Marine Corps Washington, D. C. 20380 Attn: Dr. A. L. Slafkosky Scientific Advisor (Code RD-1)	(1)
12	Defense Documentation Center Cameron Station, Building 5 Alexandria, Virginia 22314	(12)
1	Department of the Army DCS for Research, Development and Acquisition Washington, D. C. 20310 Attn: DAMA-WSA (Mr. R. L. Ballard)	(1)
1	U. S. Army Materiel Command 5001 Eisenhower Avenue Alexandria, Virginia 22333 Attn: AMCRD-F	(1)
1	Director, Ames Directorate U. S. Army Air Mobility R & D Lab Ames Research Center Moffett Field, California 94035	(1)

1	Director, Langley Directorate U. S. Army Air Mobility R & D Lab Langley Research Center Hampton, Virginia 23665	(1)
1	Director, Eustis Directorate U. S. Army Air Mobility R & D Lab Fort Eustis, Virginia 23604	(1)
1	U. S. Air Force Office of Scientific Research Building 410 Bolling AFB, D. C. 20332 Attn: Aerospace Sciences (NA)	(1)
1	U. S. Air Force Flight Dynamics Laboratory Wright-Patterson AFB, Ohio 45433 Attn: FXM, Aeromechanics Branch	(1)
2	National Aeronautics and Space Administration 600 Independence Avenue, S. W. Washington, D. C. 20546 Attn: Code RAA Code RAV	(1) (1)
1	National Aeronautics and Space Administration Ames Research Center Moffett Field, California 94035 Attn: Large-Scale Aerodynamics Branch	(1)
1	National Aeronautics and Space Administration Langley Research Center Hampton, Virginia 23665 Attn: Subsonic-Transonic Aerodynamics Division	(1)
1	Office of Naval Research Branch Office 495 Summer Street Boston, Massachusetts 02210	(1)
1	Massachusetts Institute of Technology Department of Aeronautics and Astronautics Cambridge, Massachusetts 02139 Attn: Prof. Sheila E. Widnall	(1)
1	Lockheed-Georgia Company Department 72-74, Zone 403 Marietta, Georgia 30063 Attn: Mr. Charles J. Dixon	(1)
1	RASA 1055 J. Clyde Morris Boulevard Newport News, Virginia 23602 Attn: Mr. Richard P. White	(1)
1	Nielsen Engineering & Research, Inc. 510 Clyde Avenue Mountain View, California 94043 Attn: Mr. Selden B. Spangler	(1)

UNCLASSIFIED

Security Classification

## DOCUMENT CONTROL DATA - R &amp; D

(Security classification of title, body of abstract and indexing annotation must be entered when the overall report is classified)

1. ORIGINATING ACTIVITY (Corporate author) <b>SAGE ACTION, Inc.</b> <b>P. O. Box 416</b> <b>Ithaca, New York 14850</b>		2a. REPORT SECURITY CLASSIFICATION <b>Unclassified</b>	
		2b. GROUP <b>AD-A086005</b>	
3. REPORT TITLE <b>PREDICTION OF AERODYNAMIC LOADS ON CLOSE-COUPLED CANARD CONFIGURATIONS - THEORY AND EXPERIMENT.</b>			
4. DESCRIPTIVE NOTES (Type of report and inclusive dates) <b>Final Report.</b>			
5. AUTHOR(S) (First name, middle initial, last name) <b>R. W. Hale, P. Tan and D. E. Ordway</b>			
6. REPORT DATE <b>(11) July 1977</b>		7a. TOTAL NO. OF PAGES <b>31</b>	7b. NO. OF REFS <b>9</b>
8a. CONTRACT OR GRANT NO. <b>15 N00014-72-C-0200</b>		9a. ORIGINATOR'S REPORT NUMBER(S) <b>141 SAI-RR-7702</b>	
b. PROJECT NO.		9b. OTHER REPORT NUMBER(S) (Any other numbers that may be assigned this report) <b>18 ONR-CR215-194-3F</b>	
10. DISTRIBUTION STATEMENT  <b>Approved for public release; distribution unlimited.</b>			
11. SUPPLEMENTARY NOTES		12. SPONSORING MILITARY ACTIVITY <b>Code 211</b> <b>Office of Naval Research</b> <b>Arlington, Virginia 22217</b>	
13. ABSTRACT <p>The close-coupled canard configuration has emerged as an advanced design for highly-maneuverable fighter aircraft, achieving much of its lift at high angles of attack from vortex lift. This paper summarizes the progress to date on a comprehensive investigation to develop a simplified theory for the aerodynamic performance. Flow visualization tests on a 6' (1.83 m) semi-span model of a representative configuration are first discussed. These tests are followed by measurements on a 12' (3.66 m) full-span model to obtain force and moment data, as well as pressure data on the upper surface of the wing. With this understanding, the proper velocity/vorticity relationships on the wing and the burst vortex above the wing are found and a compatible mathematical model is formulated. The general solution to the potential flow problem is then given and the influence of conical parts of the burst vortex system is derived. Numerical results for these steps look very good. In conclusion, the final steps in the development of the theory are outlined and a new mechanism for the vortex lift is identified.</p>			

DD FORM 1473 (PAGE 1)

S/N 0101-807-6801

UNCLASSIFIED

Security Classification

**Security Classification**

DD FORM 1473 (BACK)  
(PAGE 2)

**UNCLASSIFIED**  
**Security Classification**

DATE  
ILMEI  
-8



